# Micro- and nanostructured layered-kagome zinc orthovanadate BaZn 3 (VO 4 ) 2 (OH) 2

Bachchar Hadrane, Philippe Deniard, Nicolas Gautier, Michael Paris, Christophe Payen, Rémi Dessapt

ARTICLE

# Micro- and nanostructured layered-kagome zinc orthovanadate $BaZn_3(VO_4)_2(OH)_2$

Received 00th January 20xx,
Accepted 00th January 20xx

DOI: 10.1039/x0xx00000x

Bachchar Hadrane, Philippe Deniard, Nicolas Gautier, Michael Paris, Christophe Payen* and Rémi Dessapt*

Pure micro- and nanocrystalline powders of the layered-kagome zinc orthovanadate $BaZn_3(VO_4)_2(OH)_2$ have been successfully prepared and thoroughly characterised. Microstructured samples (**$BaZn_3$-MPs**) have been produced by hydrothermal reaction using synthetic martyite $Zn_3V_2O_7(OH)_2{\cdot}2H_2O$ as starting reagent. Nanoparticles (NPs) with an average size of ≈ 60 nm (**$BaZn_3$-NPs-7h**) or ≈ 50 nm (**$BaZn_3$-NPs-25min**) have been obtained by using a coprecipitation method at ambient pressure, and by varying stirring time. Rietveld refinements of X-ray diffraction data indicate that micro- and nanostructured $BaZn_3(VO_4)_2(OH)_2$ both crystallize in a $R\bar{3}m$ structure very similar to that of the known layered-kagome compound $BaCo_3(VO_4)_2(OH)_2$. Transmission electron microscopy observation of **$BaZn_3$-NPs-7h** and **$BaZn_3$-NPs-25min** reveals crystallized NPs with homogenous distributions of Ba, Zn, and V elements. FT-IR and Raman spectra show subtle differences between micro- and nanostructured samples which can not be linked to any differences in the average crystal structures. The high resolution $^{51}$V MAS NMR spectrum of **$BaZn_3$-MPs** shows a single isotropic line attributed to $VO_4^{3-}$ groups with $C_{3v}$ point group. The spectra of the nanostructured samples reveal the presence of a weak additional signal which decreases in intensity with increasing the NPs size, and which has been tentatively assigned to the presence at the surface of the NPs of a small amount of $V^{5+}$ ions in a different chemical environment. Nanostructuring also impacts the optical properties of $BaZn_3(VO_4)_2(OH)_2$. The UV-vis absorption spectra of NPs exhibit an additional weak transition in the visible domain which is not observed for the microstructured sample.

## Introduction

Orthovanadate ($VO_4^{3-}$) and pyrovanadate ($V_2O_7^{4-}$) groups are robust self-assembling units to arrange 3d transition metal ions into various lattices such as layered triangular,[1] honeycomb,[2,3] or kagome[4,5] lattices. Among them, layered-kagome materials containing divalent Cu, Co, Ni, and Zn ions offer a large variety of compositions and structures.[6–10] They have been intensively investigated these last years due to their high relevance in many domains connected to materials science including quantum magnetism,[9,11–13] visible-light driven photocatalysis,[14,15] gas sensing,[16] biosensing,[17,18] and energy storage.[19–22] In particular, the family of orthovanadates $BaM_3(VO_4)_2(OH)_2$ with M = Co, Ni, Cu has received high attention essentially because they feature kagome lattices of magnetic $M^{2+}$ centers well separated by nonmagnetic $VO_4^{3-}$ and $Ba^{2+}$ ions. Therefore, these compounds can host exotic quantum magnetic states such as quantum spin liquids. However, very little attention has been paid to their physicochemical properties and to those of their nanostructures including the optical or photocatalytic ones. $BaM_3(VO_4)_2(OH)_2$ materials contain edge-sharing distorted $[MO_4(OH)_2]$ octahedra assembled into formal $M_3O_6(OH)_2$ depleted brucite-like layers in the (*ab*) plane. As an example, the typical crystal structure of $BaCo_3(VO_4)_2(OH)_2$ (rhombohedral, $R\bar{3}m$ space group) is shown in Fig. 1.[23] The $M^{2+}$ site deficiencies are capped on both sides by $VO_4^{3-}$ groups. The layers are stacked along the *c*-axis, so that the $\mu_3$-OH groups are involved in H-bonding interaction with the terminal oxo ligand of the $VO_4$ groups of neighboring layers. Micro- and nanocrystalline powders of the synthetic analogue of the copper mineral vesignieite $BaCu_3(VO_4)_2(OH)_2$ (monoclinic, $C2/m$ space group) were intensively investigated.[4,9,24,25] This S = 1/2 kagome antiferromagnet shows a Weiss temperature θ ≈ −80 K. Micropowder samples of $BaNi_3(VO_4)_2(OH)_2$ (monoclinic, $C2/m$ space group) were then prepared by Freedman *et al*.[26] This frustrated S = 1 magnet exhibits a glassy transition at 19 K. Very recently, Li *et al.* reported the synthesis and magnetic characterisation of nanoparticles (NPs) of $BaNi_3(VO_4)_2(OH)_2$ which crystallize in the $R\bar{3}m$ space group.[27] Their magnetic properties are very different from those of the micropowder. The first synthesis of $BaCo_3(VO_4)_2(OH)_2$ was reported by Dordevic *et al.*[23] Its crystal structure was solved from small single crystals obtained under hydrothermal conditions in a mixture of other impurities. The high-spin $d^7$ $Co^{2+}$ ions form a regular kagome network, and recently, we identified this compound as a possible quantum magnet with spin–orbit coupling.[28] We reported the

*Nantes Université, CNRS, Institut des Matériaux de Nantes Jean Rouxel, IMN, F-44000 Nantes, France. E-mail : remi.dessapt@cnrs-imn.fr, christophe.payen@cnrs-imn.fr*

† Electronic Supplementary Information (ESI) available: Rietveld refinement plots, structural parameters and SEM image of $Zn_3V_2O_7(OH)_2{\cdot}2H_2O$, Rietveld refinement plot of **$BaZn_3$ NPs 25min**, structural parameters of **$BaZn_3$ NPs 25min** and **$BaZn_3$ NPs 7h**, crystal structure of $BaZn_3(VO_4)_2(OH)_2$, SEM-EDS spectrum of **$BaZn_3$ MPs**, TEM images and FFT diffraction pattern of **$BaZn_3$ NPs 25min**, TEM-EDS spectra and EDS mapping analyses of **$BaZn_3$ NPs 25min** and **$BaZn_3$ NPs 7h**. See DOI: 10.1039/x0xx00000x

synthesis and the magnetic properties of pure quasi-spherical and highly crystalline NPs of $BaCo_3(VO_4)_2(OH)_2$ with size in the range of 9–25 nm, by a simple coprecipitation method at ambient pressure, using $Ba(CH_3COO)_2$, $Co(NO_3)_2{\cdot}6H_2O$, and $NH_4VO_3$ as starting reagents.[28] The same year, Haraguchi *et al*. prepared hydrothermally microcrystalline $BaCo_3(VO_4)_2(OH)_2$ powders from a mixture of $Ba(OH)_2{\cdot}8H_2O$, $CoCl_2{\cdot}2H_2O$, and $NH_4VO_3$.[29] More recently again, we obtained pure microplatelets of $BaCo_3(VO_4)_2(OH)_2$ with variable crystallite size, by an alternative hydrothermal route, starting from microstructured synthetic karpenkoite $Co_3V_2O_7(OH)_2{\cdot}2H_2O$ as a precursor.[30] Strikingly, to the best of our knowledge, the Zn analogue of vesignieite has not been studied so far. Very recently, $BaZn_3(VO_4)_2(OH)_2$ has been mentioned as a nonmagnetic reference compound available for evaluating the lattice specific heat of $BaNi_3(VO_4)_2(OH)_2$ NPs,[27] but no structural or physicochemical characterisation data have been provided.

In this work, we report on the synthesis of pure NPs and microplatelets of $BaZn_3(VO_4)_2(OH)_2$ using synthetic routes we previously implemented to obtain nano- and microstructured $BaCo_3(VO_4)_2(OH)_2$ samples.[28,30] Microplatelets of $BaZn_3(VO_4)_2(OH)_2$ (hereafter labelled as **$BaZn_3$ MPs**) have been obtained via hydrothermal treatment of $Zn_3V_2O_7(OH)_2{\cdot}2H_2O$, which is the synthetic analogue of mineral martyite,[6] in $Ba(CH_3COO)_2$ aqueous solution. Nanostructured samples with two distinct particle sizes (hereafter labelled as **$BaZn_3$ NPs-25min** and **$BaZn_3$ NPs-7h**) were synthesised, via a coprecipitation method, by varying stirring time. All compounds have been fully characterised using X-ray diffraction (XRD), FT-IR, Raman, UV-vis, $^{51}V$ MAS NMR spectroscopies, scanning electron microscopy (SEM), transmission electron microscopy (TEM), and energy-dispersive X-ray spectroscopy (EDS) with or without elemental mapping.

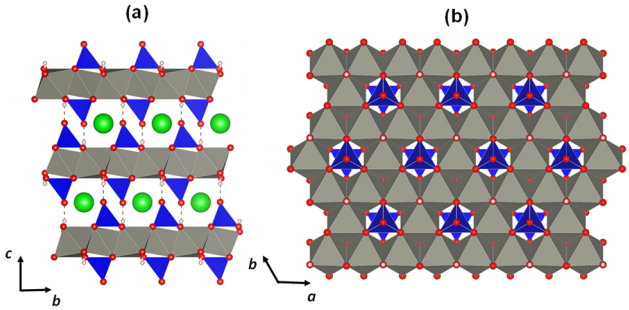


**Fig. 1** Crystal structure of $BaCo_3(VO_4)_2(OH)_2$.[23] (a) View of the (*bc*) plane. (b) View along the *c*-axis showing a fragment of a kagome layer of edge-sharing $CoO_4(OH)_2$ octahedra. Grey octahedra: $CoO_6$, blue tetrahedra: $VO_4$, red sphere: oxygen, green sphere: barium, white sphere: hydrogen. Hydrogen bonds are displayed as black dashed lines.

## Experimental

### Synthesis of micro-crystalline $BaZn_3(VO_4)_2(OH)_2$

**$BaZn_3$ MPs** was synthesized in a reproducible manner under mild hydrothermal conditions using a combination of zinc pyrovanadate $Zn_3V_2O_7(OH)_2{\cdot}2H_2O$ and aqueous barium acetate solution. First, $Zn_3V_2O_7(OH)_2{\cdot}2H_2O$ was obtained as a microcrystalline powder by a coprecipitation method at ambient pressure. An aqueous solution (4 mL) of ammonium metavanadate $NH_4VO_3$ (0.117 g - 1 mmol) was added slowly to an aqueous solution (12 mL) of $Zn(NO_3)_2{\cdot}6H_2O$ (0.446 g – 1.5 mmol) at 90 °C under vigorous magnetic stirring, leading to immediate precipitation of a white solid. The pH was adjusted to 8 by adding manually $NH_3$ (6 M), and the slurry was stirred at the same temperature for 3 hours. The mixture was then sealed in 23 mL Teflon-lined autoclave and was heated at 120 °C for 1 day. The autoclave was cooled to room temperature, and after filtration, the obtained powder was washed with water and ethanol and dried in air at room temperature. Yield in Zn = 89%. Then, 0.1 g ($2.08\ 10^{-1}$ mmol) of the as-prepared $Zn_3V_2O_7(OH)_2{\cdot}2H_2O$ was introduced into an aqueous solution (10 mL) of barium acetate $Ba(CH_3COO)_2$ (0.079 g - $3.12\ 10^{-1}$ mmol). The mixture was stirred for a few minutes under moderate heating and sealed in 23 mL Teflon-lined autoclaves, which were then heated from room temperature to 200 °C at a rate of 1 °C/min and left for 24 hours in autogenous pressure conditions. The autoclave was cooled to room temperature also at a rate of 1 °C/min. After filtration, the obtained white powder was washed with water and ethanol, and dried in air at room temperature. Yield in Zn = 85%.

### Synthesis of nanocrystalline $BaZn_3(VO_4)_2(OH)_2$

**$BaZn_3$ NPs-7h** was prepared by using a simple coprecipitation method in ambient pressure. An aqueous solution (4 mL) of $Ba(CH_3COO)_2$ (0.17 g – 0.667 mmol) was added slowly to an aqueous solution (6 mL) of $Zn(NO_3)_2{\cdot}6H_2O$ (0.298 g – 1 mmol) and $NH_4VO_3$ (0.078 g – 0.667 mmol) at 90 °C. The pH was adjusted to 8 by adding manually $NH_3$ (6M), and the mixture was maintained under vigorous magnetic stirring for 7 h. After filtration, the obtained yellowish-white powder was washed with water and ethanol, and dried in air at room temperature. A second batch of $BaZn_3(VO_4)_2(OH)_2$ NPs (hereafter labelled as **$BaZn_3$ NPs-25min**) was obtained according to a similar synthesis procedure, except for the stirring time which was limited to 25 min. Yields in Zn were 47% and 93% for **$BaZn_3$ NPs-25min** and **$BaZn_3$ NPs-7h**, respectively.

### Characterisation Methods

SEM images and EDS spectra were obtained with a JEOL JSM 7600F and JEOL JSM 5800LV scanning electron microscopes, respectively. EDS analyses were carried out on thin pellets for **$BaZn_3$ MPs**. XRD measurements were performed on a D8 Bruker diffractometer employing the CuK-L3 radiation (Ge (111) monochromator) and a Lynxeye 1D detector in the 5–110° 2θ interval, with 0.014° steps of 3 s each. Structure refinements were carried out with the Jana2020 software,[31] using the Rietveld procedure with the fundamental parameter approach.[32] This approach makes possible the deconvolution of the X-ray line profile diffractometer without the need for a standard: X-ray energy dispersion and optics in one hand and the specimen itself in the other hand. The estimated standard deviations were calculated in agreement with the procedure reported by Berar *et al.*[33] Nitrogen volumetric measurement treated by the Brunauer-Emmett-Teller (BET) approaches were recorded on a micrometrics ASAP 2010 device. Fourier transform infrared (FT-IR) spectra were recorded at room temperature, using the conventional transmission technique in KBr-pellets, in the 4000-400 $cm^{-1}$ range on a BRUKER Vertex equipped with a computer control using the OPUS software. Room-temperature Raman spectra were collected under microscope in backward scattering configuration using a

Renishaw InVia spectrometer and the 514 nm line of an argon ion laser. The laser probe diameter at the sample surface was approximately 2 µm. The laser power was reduced to about 0.1 mW to avoid sample heating. Two edge filters were used to filter the Rayleigh line intensity, allowing measurements above 100 $cm^{-1}$. Spectra were recorded at 2 $cm^{-1}$ resolutions over the wavenumber range -20-1900 $cm^{-1}$, with 10 scan accumulation (with 10 s as exposure time per scan). Scanning transmission microscopy and EDS mapping were performed with a Themis Z G3 (Thermo Fisher Scientific) operated at 300 kV. NPs were dispersed in ethanol using ultrasonication and then deposited on a gold grid covered with a thin carbon film. Electron diffraction patterns were compared to those simulated using the JEMS software (https://www.jems-swiss.ch/). Diffuse reflectance spectra were collected at room temperature on a finely ground sample with a Perkin-Elmer Lambda 1050 spectrometer equipped with a 150 mm diameter integrating sphere coated with Spectralon®, a highly reflecting fluoropolymer. Diffuse reflectance was measured from 250 to 850 nm with a 2 nm step using Spectralon® as reference (100% reflectance). The reflectance data were treated by a Kubelka-Munk transformation[34] to determine the absorption thresholds. $^{51}V$ MAS (Magic Angle Spinning) NMR spectra were acquired on a 500 MHz Bruker spectrometer equipped with a 2.5 mm MAS probe. We used a single $\pi/15$ pulse excitation with a radiofrequency field of 110 kHz. MAS frequency was set to 20 kHz and the delay between scans to 1 s. Baseline were corrected using the tool developed by Yon *et al*.[35] Spectra were referenced with respect to $VOCl_3$ by using $Na_3VO_4$ as a secondary reference at -545 ppm.[36]

## Results and discussion

First, a Rietveld refinement of the XRD pattern of the $Zn_3V_2O_7(OH)_2{\cdot}2H_2O$ powder sample which was used as starting reagent for the synthesis of **$BaZn_3$ MPs** was successfully performed using the published $P\bar{3}m$ structural model.[37] The final Rietveld plot is shown in Fig. S1, ESI†, and the refined structural parameters are gathered in Table S1, ESI†. The refined crystallite size is 109(2) nm. The microplatelet morphology of $Zn_3V_2O_7(OH)_2{\cdot}2H_2O$ was well evidenced by SEM (Fig. S2, ESI†).

Then, the purity and crystallinity of the micro- and nanostructured $BaZn_3(VO_4)_2(OH)_2$ samples were confirmed by XRD analyses at room temperature. Since XRD patterns compared well with ICSD card no. 236321 for $BaCo_3(VO_4)_2(OH)_2$, all patterns were refined starting from the published $R\bar{3}m$ structural model.[23] Final Rietveld plots for **$BaZn_3$ MPs** and **$BaZn_3$ NPs-7h** are shown in Fig. 2. Fig. S3, ESI† displays the Rietveld plot for **$BaZn_3$ NPs-25min**. Refined structural parameters and crystallite sizes of **$BaZn_3$ MPs**, **$BaZn_3$ NPs-7h**, and **$BaZn_3$ NPs-25min** are listed in Table 1, Tables S2 and S3, ESI†, respectively. Principal bond lengths for all samples are given in Table S4, ESI†. The refined crystallite size is of 185(5) nm for **$BaZn_3$ MPs**. These results indicate that this compound is isostructural with $BaCo_3(VO_4)_2(OH)_2$,[23,28,30] the crystal structure of which has been described in the introduction and presented in Fig. 1. Ba atoms have 12-fold coordination with 6 short Ba-O2 = 2.81 Å (Fig. S4, ESI†), and 6 six long Ba-O1 = 3.45 Å distances. Zn and V atoms reside on site of 2/m and 3m symmetry, respectively. $ZnO2_4O3_2$ octahedra and $VO2_3O1$ tetrahedra are distorted (Fig. S4, ESI†). The Zn atoms are coordinated to four equatorial oxygen atoms, with Zn-O2 = 2.23 Å, and two axial O3-H hydroxide ligands, with Zn-O3 = 1.95 Å. Within the orthovanadate group, the V-O1 bond (V-O1 = 1.67 Å) is stronger than the V-O2 bond (V-O2 = 1.71 Å), so that the $VO_4$ unit adopts a $C_{3v}$ point group. **$BaZn_3$ NPs-7h** exhibits anisotropic crystallite sizes of 26.0(8) nm along the *c*-axis, and of 37(2) nm perpendicular to the *c*-axis. For **$BaZn_3$ NPs-25min**, crystallite sizes are 13.1(4) nm along the *c*-axis, and 19.3(1) nm perpendicular to the *c*-axis. As expected, the crystallite size increases with stirring time.

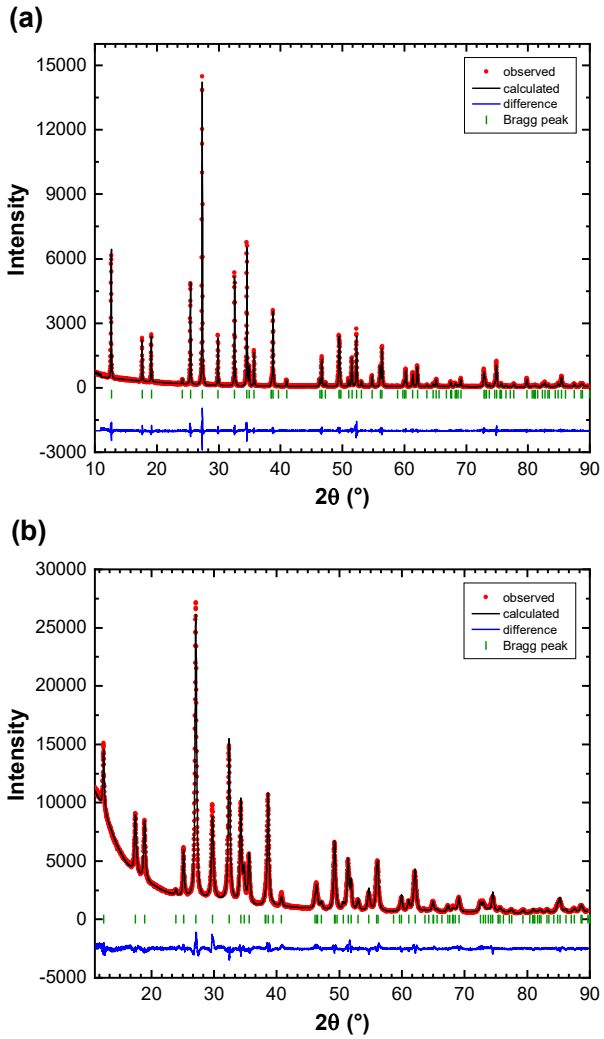


**Fig. 2** Rietveld refinement plots for (a) **$BaZn_3$ MPs**, and (b) **$BaZn_3$ NPs-7h**, showing observed, calculated and difference patterns.

An important outcome of our Rietveld refinements is that the average crystal structure is not affected by the synthesis route or by the crystallite size. This can be seen in Tables S2 and S3, ESI†, which gather cell parameters and atom positions for **$BaZn_3$ NPs-7h** and **$BaZn_3$ NPs-25min**, and in Table S4, ESI†, which gives the main interatomic distances for **$BaZn_3$ MPs** and for the two nanostructured samples. Taking into account the

uncertainties, the individual and mean Ba-O, Zn-O, and V-O bond distances do not change when the crystallite sizes decrease.

**Table 1** Structural parameters, final agreement factors, and crystallite sizes for **$BaZn_3$ MPs.**

| S.G. $R\bar{3}m$ : a (Å) = 5.9732(2), c (Å) = 20.9890(6)<br>Cryst. Size = 185(5) nm | | | | | |
|---|---|---|---|---|---|
| Atom | x | Y | z | SOF | $U_{iso}$ Equiv (Å$^2$) |
| $Ba_1$ | 2/3 | 1/3 | 5/6 | 1 | 0.060(2) |
| $Zn_1$ | 5/6 | 2/3 | 2/3 | 1 | 0.050(3) |
| $V_1$ | 1/3 | 2/3 | 0.7555(3) | 1 | 0.041(3) |
| $O_1$ | 1/3 | 2/3 | 0.8349(9) | 1 | 0.041(3) |
| $O_2$ | 0.491(2) | 0.509(2) | 0.7313(4) | 1 | 0.041 |
| $O_3$ | 1 | 1 | 0.7098(11) | 1 | 0.041 |
| $H_1$ | 1 | 1 | 0.7494* | 1 | 0.008* |
| GOF=1.81, Rp= 8.31, and Rwp= 11.34 | | | | | |

| | $U_{11}$ | $U_{22}$ | $U_{33}$ | $U_{12}$ | $U_{13}$ | $U_{23}$ |
|---|---|---|---|---|---|---|
| $Ba_1$ | 0.076(3) | 0.076 | 0.029(3) | 0.038(2) | 0 | 0 |
| $Zn_1$ | 0.054(3) | 0.053(4) | 0.044(3) | 0.026(2) | -0.001(2) | -0.002(3) |
| $V_1$ | 0.046(4) | 0.046 | 0.033(4) | 0.023(2) | 0 | 0 |

*not refined

The particle shapes and sizes of **$BaZn_3$ MPs**, **$BaZn_3$ NPs-7h** and **$BaZn_3$ NPs-25min** were initially revealed by SEM (Fig. 3). **$BaZn_3$ MPs** consists of microplatelets with sizes in the approximate range of 0.5–10 µm (Fig. 3(a) and 3(b)). Zn/Ba, V/Ba and Zn/V elemental ratios were determined by SEM-EDS analyses (Fig. S5, ESI†) and were equal to 3.2(2), 2.1(2) and 1.5(1), respectively, in good agreement with the expected ones. The microstructured powder exhibits a very low specific surface area of about 3.2 m$^2$ g$^{-1}$ which compares well to that observed for microplatelets of $BaCo_3(VO_4)_2(OH)_2$ (2.2 m$^2$ g$^{-1}$) that we recently elaborated by a similar hydrothermal procedure.[30] **$BaZn_3$ NPs-7h** and **$BaZn_3$ NPs-25min** are composed of NPs with size distribution in the range of 40–70 nm (Fig. 3(c) and 3(d)) and of 35-80 nm (Fig. 3(e) and 3(f)), respectively**.** As expected, the specific surface areas of **$BaZn_3$ NPs-7h** (20.7 m$^2$ g$^{-1}$) and **$BaZn_3$ NPs-25min** (11.9 m$^2$ g$^{-1}$) nanopowders are higher than that of **$BaZn_3$ MPs**. These values are smaller than that recently reported for $BaCo_3(VO_4)_2(OH)_2$ NPs (61 m$^2$ g$^{-1}$) with a smaller average particle size of ≈ 20 nm.[28] The rather low specific surface area for **$BaZn_3$ NPs-25min** is likely explained by the formation of aggregates, which are assemblies of primary particles with size distribution in the range of 35-80 nm (Fig. 3(e)). For **$BaZn_3$ MPs-7h**, an average particle diameter (*d*) can be calculated from the specific surface area (*S*) using the formula $d$(nm) = $6.10^3/[\rho(cm^3/g)\times S(m^2/g)]$, where $\rho$ is the density deduced from Rietveld refinement. It yields *d* = 63 nm, consistent with the particle size histogram deduced from SEM (Fig. 3(d)). Next, **$BaZn_3$ NPs-7h** and **$BaZn_3$ NPs-25min** were characterised by STEM (Fig. 4 and Fig. S6, ESI†). STEM images confirmed the SEM observation of size and shapes, and revealed that NPs are well crystallized. For both samples, FFT diffraction patterns have been indexed using the $R\bar{3}m$ model derived from the Rietveld refinements of XRD data. EDS mapping analyses for Ba, Zn, V (Fig. S7 and S8, ESI†) indicate homogeneous distributions of these elements. The calculated Zn/Ba, V/Ba and Zn/V elemental ratios were found to be 2.8(1), 2.3(4), and 1.2(2), respectively.

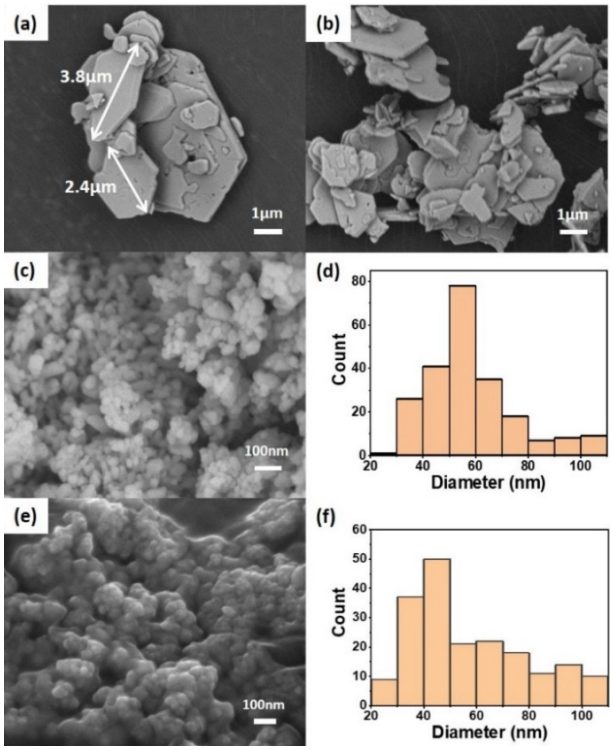


**Fig. 3** SEM images of (a, b) **$BaZn_3$ MPs**, (c) **$BaZn_3$ NPs-7h**, and (e) **$BaZn_3$ NPs-25min**. Particle size histograms for (d) **$BaZn_3$ NPs-7h** and (f) **$BaZn_3$ NPs-25min**.

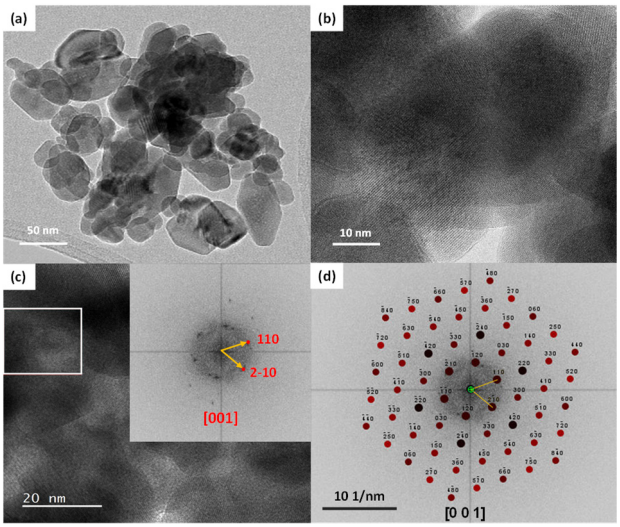


**Fig. 4** (a,b) TEM images of representative **$BaZn_3$ NPs-7h** at different magnifications. Reticular planes are visible in (b). (c,d) FFT diffraction pattern along the [001] zone axis from the region marked out by the white rectangle in (c). Global indexing in (d) was obtained using the structural model deduced from XRD (Table S2, ESI†).

In order to probe the local structures, the micro- and nanostructured compounds were characterised by FT-IR and Raman spectroscopies (Fig. 5). The FT-IR spectrum of **$BaZn_3$ MPs** (Fig. 5(a)) shows four intense bands at 970, 934, 802 and 741 cm$^{-1}$ which have been assigned to the stretching modes of orthovanadate $VO_4^{3-}$ groups with

$C_{3v}$ point group,[38] probably coupled with V-O-Zn modes. A less intense band at 513 $cm^{-1}$ has been attributed to a Zn-O stretching mode. The broad band at 2963 $cm^{-1}$ can be assigned to the stretching mode of the $\mu_3$-OH groups of the kagome layers, while the very weak broad band at 3451 $cm^{-1}$ characterises νOH stretching modes of traces of adsorbed water molecules. The weak band at 1867 $cm^{-1}$ may be assigned to combination and overtone modes. Interestingly, the FT-IR spectra of **$BaZn_3$ NPs-7h** and **$BaZn_3$ NPs-25min** are very similar to each other, but exhibit significant differences with that of **$BaZn_3$ MPs**. Indeed, in the range of 4000-2000 $cm^{-1}$, the broad band relative to νOH stretching modes of water molecules at 3450 $cm^{-1}$ is much more intense for **$BaZn_3$ NPs-7h** and **$BaZn_3$ NPs-25min**, and a weak band at 1634 $cm^{-1}$ relative to the HOH bending modes is also clearly distinguishable. This is well consistent with an expected increase in amount of adsorbed water at the surface of the nanostructured samples. Moreover, the IR signature of the layered-kagome orthovanadate is also impacted by nanostructuring. The V-O and V-O-Zn modes are characterised by four bands at 970, 905, 791, and 758 $cm^{-1}$, and the stretching mode of the $\mu_3$-OH groups is shifted to 2974 $cm^{-1}$. In contrast, the energy of the Zn-O stretching mode (513 $cm^{-1}$) is similar to that observed for **$BaZn_3$ MPs**. Let us notice that the IR spectra of the $BaZn_3(VO_4)_2(OH)_2$ compounds are perfectly comparable with those of the micro- and nanostructured samples of their Co analogues.[28,30] These differences in vibrational spectroscopy signatures between micro- and nanostructured $BaM_3(VO_4)_2(OH)_2$ (M = Zn, Co) cannot be explained by differences in the average crystal structures as determined by Rietveld refinements of XRD data.

Attribution of vibrational Raman bands of **$BaZn_3$ MPs** (Fig. 5(b)) have been tentatively done by comparison with the Raman signatures of reported $BaM_3(VO_4)_2(OH)_2$ (M = Cu,[38] Co[28]) samples. **$BaZn_3$ MPs** exhibit two intense bands at 883 and 807 $cm^{-1}$, and two much less intense ones at 969 and 717 $cm^{-1}$, relative to the $\nu_1$ symmetric and $\nu_3$ antisymmetric stretching modes of the orthovanadate units with $C_{3v}$ point group. The weakly intense band at 470 $cm^{-1}$ could be ascribed to the $\nu_4$ $(VO_4)^{3-}$ antisymmetric bending modes, and the two other more intense bands at 360 and 322 $cm^{-1}$ have been assigned to the $\nu_2$ symmetric bending modes. Noticeably, the broadening of the Raman peaks increases with decreasing the particle size, indicating that the Raman signature profile of $BaZn_3(VO_4)_2(OH)_2$ is strongly impacted by nanostructuring, in perfect agreement with what we recently observed for micro- and nanostructured $BaCo_3(VO_4)_2(OH)_2$ samples.[28,30]

High resolution $^{51}V$ MAS NMR spectroscopy was also used as a local probe of the crystal structure. Fig. 6 shows the NMR spectra of **$BaZn_3$ MPs**, **$BaZn_3$ NPs-7h**, and **$BaZn_3$ NPs-25min**. As expected from the crystal structure, a single isotropic line is observed for **$BaZn_3$ MPs**. Its position at -546 ppm is within the range of isotropic chemical shifts usually observed for orthovanadate groups.[39]

For **$BaZn_3$ NPs-7h** and **$BaZn_3$ NPs-25min**, a strong signal at the same position is also observed, confirming the same environment for $VO_4^{3-}$ groups in both micro- and nanoparticles, in agreement with XRD results (see above). The comparison of the three spectra echoes what is observed by Raman spectroscopy i.e., linewidths increase as the particle size decreases (see inset in Fig. 6).

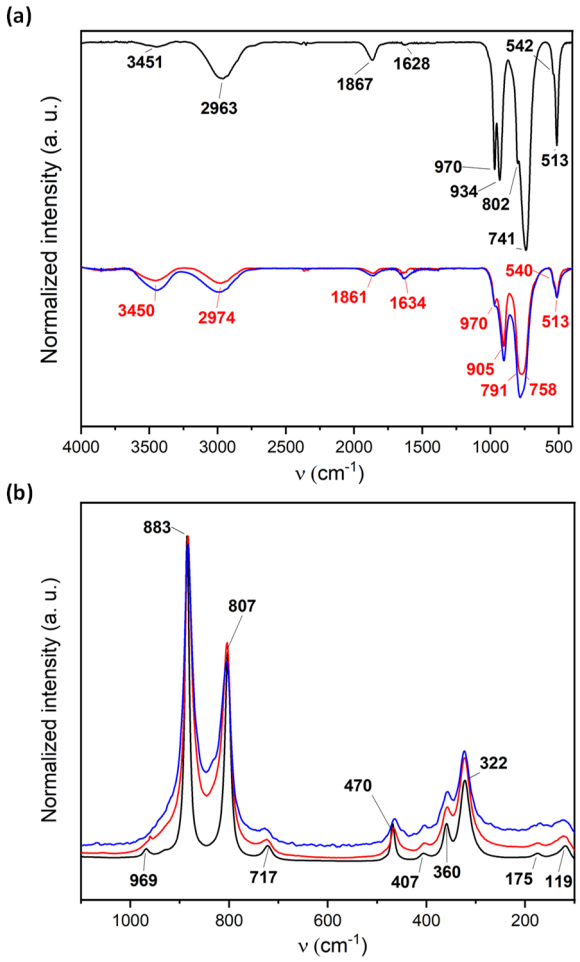


**Fig. 5** Comparison of (a) FT-IR and (b) Raman spectra of **$BaZn_3$ MPs** (black line), **$BaZn_3$ NPs-7h** (red line), and **$BaZn_3$ NPs-25min** (blue line).

Moreover, the spinning side bands manifolds stemming from $^{51}V$ satellite transitions expand farther for nanoparticles. Hence, the nanoparticles appear less well-crystallized than microparticles, but still homogeneous. If not, the spectra of the nanoparticles would present the superimposition of two lines, one broad and one thin, revealing then a core-shell structure. For **$BaZn_3$ NPs-7h** and **$BaZn_3$ NPs-25min** only, an additional weak line around –566 ppm is observed. However, the weak line is broader than the main one, and the associated quadrupolar coupling constant ($C_Q$) is also larger (as shown by the inspection of the outermost spinning side bands). This suggests that a small amount of vanadium ions is localized in a more distorted environment. Finally, the ratio between the weak line and the main line is larger for **$BaZn_3$ NPs-25min** than for **$BaZn_3$ NPs-7h**. In addition, the ratio does not change after washing the nanostructured samples several times with water and ethanol. Therefore, we have tentatively attributed the weak and broad signal around -566 ppm to the presence at the surface of the NPs of $V^{5+}$ ions in a chemical environment different from that of the bulk.

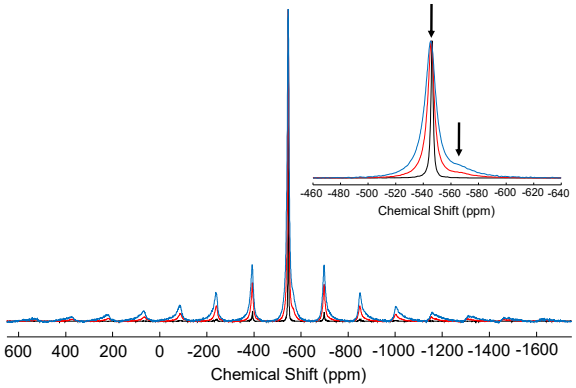


**Fig. 6** $^{51}$V MAS NMR spectra of **$BaZn_3$ MPs** (black line), **$BaZn_3$ NPs-7h** (red line), and **$BaZn_3$ NPs-25min** (blue line). Insert represents an enlargement of the isotropic chemical shift lines around -566 ppm and -546 ppm (indicated by black arrows) showing different broadening.

Since the color of micro- and nanocrystalline $BaZn_3(VO_4)_2(OH)_2$ differ, their solid-state absorption properties were investigated by diffuse reflectance spectroscopy. Fig. 7 shows the Kubelka–Munk transformed reflectivity spectra of **$BaZn_3$ MPs** and **$BaZn_3$ NPs-7h**. **$BaZn_3$ NPs-25min** shows the same behaviour as that of **$BaZn_3$ NPs-7h**. The intense absorption bands in the range of 250-350 nm can be ascribed to mixed O→V and O→Zn ligand-to-metal charge-transfer transitions.[40] Optical band gap (Eg) energies are 3.56 eV, 3.55 eV, and 3.54 eV for **$BaZn_3$ MPs**, **$BaZn_3$ NPs-7h**, and **$BaZn_3$ NPs-25min**, respectively. Unlike in **$BaZn_3$ MPs**, a weak absorption band shows up in the visible region for the NPs, consistent with their slight colouring shown in the inset of Fig. 7, which is maintained even after washing the samples several times with water and ethanol. Let us notice that this colour is consistent with that previously mentioned for a powder with an unknown particle size.[27]

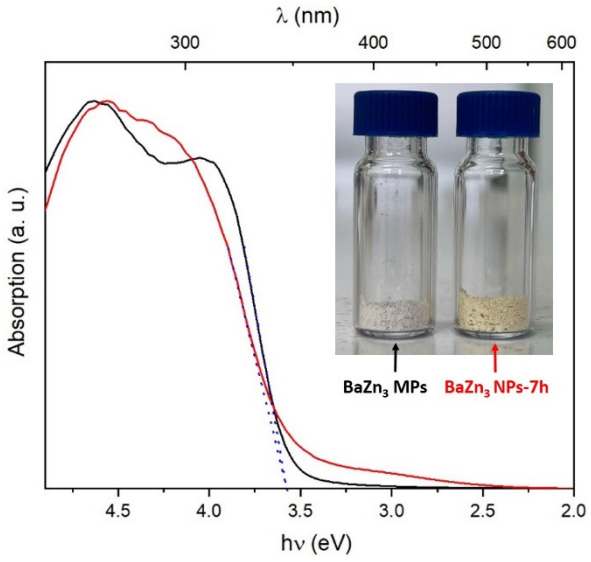


**Fig. 7** Kubelka–Munk transformed reflectance spectra of **$BaZn_3$ MPs** (black line) and **$BaZn_3$ NPs-7h** (red line). The blue dashed lines denote the linear parts of the plots, which are extrapolated to the x-axis. Inset: Photographs of the corresponding powdered samples.

It is tempting to ascribe this additional absorption band to nanostructure-induced $V^{5+}$ species that yield the weak additional line in the $^{51}$V NMR spectra (see above). However, at this stage of our study, there is no evidence to support such an assumption. The nanostructure-induced optical absorption could also be ascribed to the presence of defects or pending bonds of unknown origin.

## Conclusions

In summary, we successfully elaborated micro- and nanocrystalline powders of the layered-kagome $BaZn_3(VO_4)_2(OH)_2$ compound which completes well the series already known for M = Cu, Co, and Ni. As for its Co and Cu analogues, microplatelets of $BaZn_3(VO_4)_2(OH)_2$ could be prepared using the layered-kagome pyrovanadate $ZnV_2O_7(OH)_2{\cdot}2H_2O$ as starting reagent. NPs of $BaZn_3(VO_4)_2(OH)_2$ with two distinct particle sizes were also obtained using a coprecipitation method similar to that earlier used for elaborating nanostructured $BaCo_3(VO_4)_2(OH)_2$. Microstructured $BaZn_3(VO_4)_2(OH)_2$ is isostructural with $BaCo_3(VO_4)_2(OH)_2$. Average crystal structures of micro and nanostructured $BaZn_3(VO_4)_2(OH)_2$ as revealed by XRD are the same within error. Nonetheless, differences in local structures due to nanostructuring have been evidenced by FT-IR, Raman and $^{51}$V MAS NMR spectroscopies. In particular, the nanostructured powders contain small amount of $V^{5+}$ ions in a chemical environment which differs from distorted $VO_4^{3-}$ tetrahedra with $C_{3v}$ point group, as observed in the bulk sample. Nanostructuring also induces optically active defects which significantly modify the absorption properties of $BaZn_3(VO_4)_2(OH)_2$. Finally, considering that the crystal structures of $BaZn_3(VO_4)_2(OH)_2$ and of its Cu, Co, and Ni counterparts are topologically similar, our works open the possibility of elaborating new solid solutions with highly tunable photophysical and magnetic properties.

## Author Contributions

The manuscript was written through contributions of all authors. All authors have given approval to the final version of the manuscript.

## Conflicts of interest

There are no conflicts to declare.

## Acknowledgements

This work was supported by Nantes Université, the CNRS, and the Ministère de l'Enseignement Supérieur et de la Recherche. The CIMEN Electron Microscopy Center in Nantes is also greatly acknowledged.

## Notes and references

1 L. D. Sanjeewa, V. O. Garlea, M. A. McGuire, M. Frontzek, C. D. McMillen, K. Fulle and J. W. Kolis, *Inorg. Chem.*, 2017, **56**, 14842–14849.
2 Liurukara. D. Sanjeewa, M. A. McGuire, C. D. McMillen, D. Willett, G. Chumanov and J. W. Kolis, *Inorg. Chem.*, 2016, **55**, 9240–9249.
3 J. Sannigrahi, D. T. Adroja, R. Perry, M. J. Gutmann, V. Petricek and D. Khalyavin, *Phys. Rev. Mater.*, 2019, **3**, 113401.
4 M. Yoshida, Y. Okamoto, M. Takigawa and Z. Hiroi, *J. Phys. Soc. Jpn.*, 2013, **82**, 013702.
5 M. A. Lafontaine, A. Le Bail and G. Férey, *J. Solid State Chem.*, 1990, **85**, 220–227.
6 A. R. Kampf and I. M. Steele, *Can. Mineral.*, 2008, **46**, 687–692.
7 I. V. Pekov, O. I. Siidra, N. V. Chukanov, V. O. Yapaskurt, S. N. Britvin, S. V. Krivovichev, W. Schüller and B. Ternes, *Mineral. Petrol.*, 2015, **109**, 705–711.
8 A. V. Kasatkin, J. Plasil, I. V. Pekov, D. I. Belakovskiy, F. Nestola, J. Cejka, M. F. Vigasina, F. Zorzi and B. Thorne, *J. Geosci.*, 2015, **60**, 251–257.
9 Y. Okamoto, H. Yoshida and Z. Hiroi, *J. Phys. Soc. Jpn.*, 2009, **78**, 033701.
10 D. Boldrin and A. S. Wills, *J. Mater. Chem. C*, 2015, **3**, 4308–4315.
11 H. Ishikawa, D. Nishio-Hamane, A. Miyake, M. Tokunaga, A. Matsuo, K. Kindo and Z. Hiroi, *Phys. Rev. Mater.*, 2019, **3**, 064414.
12 H. Ishikawa, M. Yoshida, K. Nawa, M. Jeong, S. Krämer, M. Horvatic, C. Berthier, M. Takigawa, M. Akaki, A. Miyake, M. Tokunaga, K. Kindo, J. Yamaura, Y. Okamoto and Z. Hiroi, *Phys. Rev. Lett.*, 2015, **114**, 227202.
13 A. Zorko, F. Bert, A. Ozarowski, J. van Tol, D. Boldrin, A. S. Wills and P. Mendels, *Phys. Rev. B*, 2013, **88**, 144419.
14 P. Wang, H. Yang, D. Wang, A. Chen, W.-L. Dai, X. Zhao, J. Yang and X. Wang, *Phys. Chem. Chem. Phys.*, 2018, **20**, 24561–24569.
15 Y. Song, X. Zhao, X. Feng, L. Chen, T. Yuan and F. Zhang, *ACS Appl. Energy Mater.*, 2022, **5**, 10542–10552.
16 K. Hua, M. Cui, Z. Luo, D. Fang, R. Bao, Q. Qi, J. Yi, B. Sun and C. Chen, *J. Alloys Compd*, 2019, **801**, 581–588.
17 S. Jain, B. Sharma, N. Thakur, S. Mishra and T. K. Sarma, *ACS Appl. Nano Mater.*, 2020, **3**, 7917–7929.
18 Y. Liu, P. Hao, Z. Liu, G. Li, G. Fan, M. Xie and Q. Liu, *Analyst*, 2023, **148**, 269–277.
19 L. Chen, Z. Yang, J. Wu, H. Chen and J. Meng, *Electrochim. Acta*, 2020, **330**, 135347.
20 C. Xia, J. Guo, Y. Lei, H. Liang, C. Zhao and H. N. Alshareef, *Adv. Mater.*, 2018, **30**, 1705580.
21 G. Yang, S. Li, M. Wu and C. Wang, *J. Mater. Chem. A*, 2016, **4**, 10974–10985.
22 A. Chowdhury, R. Shukla, V. Sharma, S. Neogy, A. Chandra, V. Grover and A. K. Tyagi, *J. Alloys Compd*, 2020, **829**, 154479.
23 T. Dordević and L. Karanović, *Acta Crystallogr., Sect. C: Cryst. Struct. Commun.*, 2013, **69**, 114–118.
24 D. Boldrin, K. Knight and A. S. Wills, *J. Mater. Chem. C*, 2016, **4**, 10315–10322.
25 D. Boldrin, B. Fåk, E. Canévet, J. Ollivier, H. C. Walker, P. Manuel, D. D. Khalyavin and A. S. Wills, *Phys. Rev. Lett.*, 2018, **121**, 107203.
26 D. E. Freedman, R. Chisnell, T. M. McQueen, Y. S. Lee, C. Payen and D. G. Nocera, *Chem. Commun.*, 2012, **48**, 64–66.
27 B. Li, Z. Wan, Y. Song, Z. Ma, Y. Zhao, J. Wang and Y. Li, *J. Phys.: Condens. Matter*, 2023, **35**, 505801.
28 R. Dessapt, L. Lajaunie, J. J. Calvino, P. Deniard, I. Trenque and C. Payen, *J. Mater. Chem. C*, 2022, **10**, 3287–3291.
29 Y. Haraguchi, T. Ohnoda, A. Matsuo, K. Kindo and H. A. Katori, *Phys. Rev. B*, 2022, **106**, 214421.
30 B. Hadrane, P. Deniard, C. Jeannot, I. Trenque, R. Dessapt and C. Payen, *Dalton Trans.*, 2023, **52**, 3501–3507.
31 V. Petricek, M. Dusek and L. Palatinus, *Z. Kristallogr.*, 2014, **229**, 345–352.
32 R. W. Cheary and A. Coelho, *J. Appl. Crystallogr.*, 1992, **25**, 109–121.
33 J.-F. Bérar and P. Lelann, *J. Appl. Crystallogr.*, 1991, **24**, 1–5.
34 P. Kubelka and F. Munk, *Z. Techn. Physik*, 1931, **12**, 593–601.
35 M. Yon, F. Fayon, D. Massiot and V. Sarou-Kanian, *Solid State Nucl. Magn. Reson.*, 2020, **110**, 101699.
36 H. Eckert and I. E. Wachs, *J. Phys. Chem.*, 1989, **93**, 6796–6805.
37 P. Y. Zavalij, F. Zhang and M. S. Whittingham, *Acta Cryst C*, 1997, **53**, 1738–1739.
38 R. L. Frost, S. J. Palmer, J. Čejka, J. Sejkora, J. Plášil, S. Bahfenne and E. C. Keeffe, *J. Raman Spectrosc.*, 2011, **42**, 1701–1710.
39 O. B. Lapina, V. M. Mastikhin, A. A. Shubin, V. N. Krasilnikov and K. I. Zamaraev, *Prog. Nucl. Magn. Reson. Spectrosc.*, 1992, **24**, 457–525.
40 A. Bayat, A. R. Mahjoub and M. M. Amini, *J. Math. Sci.*, 2018, **29**, 2915–2926.